

Theory of successive transitions in vanadium spinels and order of orbitals and spins

Yukitoshi MOTOME¹ and Hirokazu TSUNETSUGU²

¹*RIKEN (The Institute of Physical and Chemical Research), Saitama 351-0198*

²*Yukawa Institute for Theoretical Physics, Kyoto University, Kyoto 606-8502*

We have theoretically studied successive transitions in vanadium spinel oxides with $(t_{2g})^2$ electron configuration. These compounds show a structural transition at $\sim 50\text{K}$ and an antiferromagnetic transition at $\sim 40\text{K}$. Since threefold t_{2g} orbitals of vanadium cations are occupied partially and vanadiums constitute a geometrically-frustrated pyrochlore lattice, the system provides a particular example to investigate the interplay among spin, orbital and lattice degrees of freedom on frustrated lattice. We examine the models with the Jahn–Teller coupling and/or the spin–orbital superexchange interaction, and conclude that keen competition between these two contributions explains the thermodynamics of vanadium spinels. Effects of quantum fluctuations as well as relativistic spin–orbit coupling are also discussed.

§1. Introduction

In this paper, we review our recent studies on phase transitions in vanadium spinel compounds, AV_2O_4 ($A=\text{Zn, Mg or Cd}$).^{1)–5)} This family of materials is antiferromagnetic insulator with spin $S = 1$ on pyrochlore sublattice in the spinel structure (Fig. 1). Recent experiments showed the presence of two successive phase transitions at low temperatures around 50K .⁶⁾ As temperature is lowered, a structural transition occurs first, then a magnetic transition follows. As we will discuss later, simple spin exchange mechanism does not explain the lowest temperature phase, and we need to take account of two important factors in order to explain basic character of these transitions. One is geometrical frustration and the other is strong correlation effects, which lead to keen competition of various degrees of freedom. As widely known, the geometrical frustration often leads to huge degeneracy of the ground-state manifold, and suppresses a long-range ordering. On the other hand, the strong electron correlation opens several channels in the low energy sector, such as spin and orbital degrees of freedom. A key question is how these channels affect the manifold — do they result in some nontrivial phenomena through enhanced fluctuations, or lift the degeneracy in some nontrivial manner? We would like to clarify this intriguing problem by studying effects of both frustration and correlation in the vanadium spinels.

Vanadium spinels are a $3d$ -electron system with orbital degrees of freedom. In the last decade, various transition-metal materials have been intensively studied to investigate the effects of orbital degrees of freedom.⁷⁾ In particular, manganites showing colossal magnetoresistance (CMR) are the most typical example. Vanadium spinels have different features from these materials. A distinct difference is the lattice structure. In manganites showing CMR, the lattice structure is perovskite; atomic bonds are connected with right angle and the network of magnetic ions is close to a

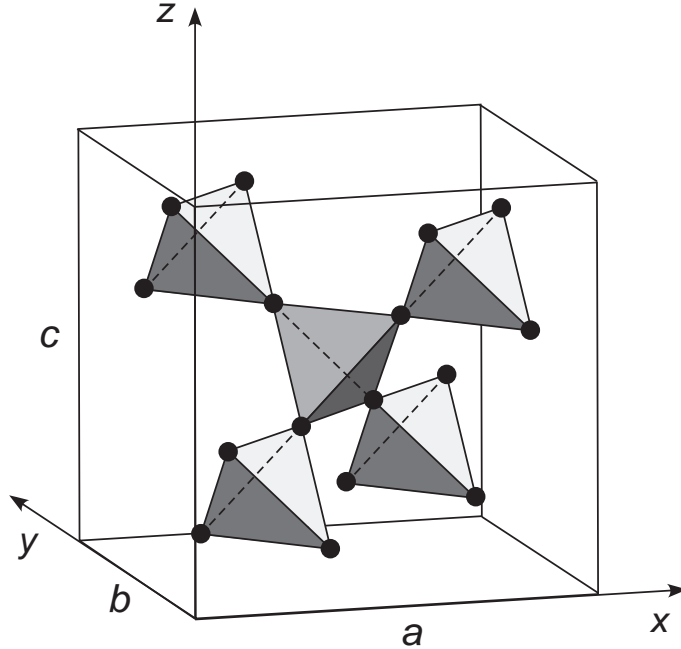


Fig. 1. Cubic unit cell of the pyrochlore lattice. In vanadium spinels, vanadium cations constitute this pyrochlore structure.

simple cubic lattice. In spinels, atomic bonds are connected to constitute a lattice in which elementary plaquettes are triangles; the network of magnetic cations is the pyrochlore lattice shown in Fig. 1. Another important difference is that the vanadates are a t_{2g} -electron system, whereas the manganites have conduction electrons in e_g multiplet. Jahn–Teller distortions are generally smaller in t_{2g} systems, and the crystal-field splitting of the electronic levels is less prominent, partly because t_{2g} orbitals point away from surrounding anions. Therefore, it is important to take account of orbital degrees of freedom in t_{2g} systems like vanadium spinels. We also note that t_{2g} electrons may have a nonzero orbital angular momentum, whereas orbital angular momenta are quenched in e_g systems. This also leads to several effects present only in t_{2g} systems. For example, relativistic spin–orbit coupling is sometimes important to take into account, but this is not a central issue in this paper.

From the viewpoints of orbital physics and geometrical frustration, spinels with transition-metal ions are very interesting system. In this paper, we shall discuss about two phase transitions in vanadium spinels with divalent A -site cations such as Zn, Mg or Cd. In these materials, first of all, interesting phenomena such as phase transitions occur at much lower temperatures compared to a typical energy scale in the system. That is, the characteristic energy scale, which is given by, for example, the Curie–Weiss temperature estimated from the temperature dependence of the magnetic susceptibility, is $\sim 1000\text{K}$,⁸⁾ nevertheless the system remains paramagnetic and does not show any transition down to $\sim 50\text{K}$. This suppression of relevant energy scale is characteristic to frustrated systems. At low temperatures, in the end, the

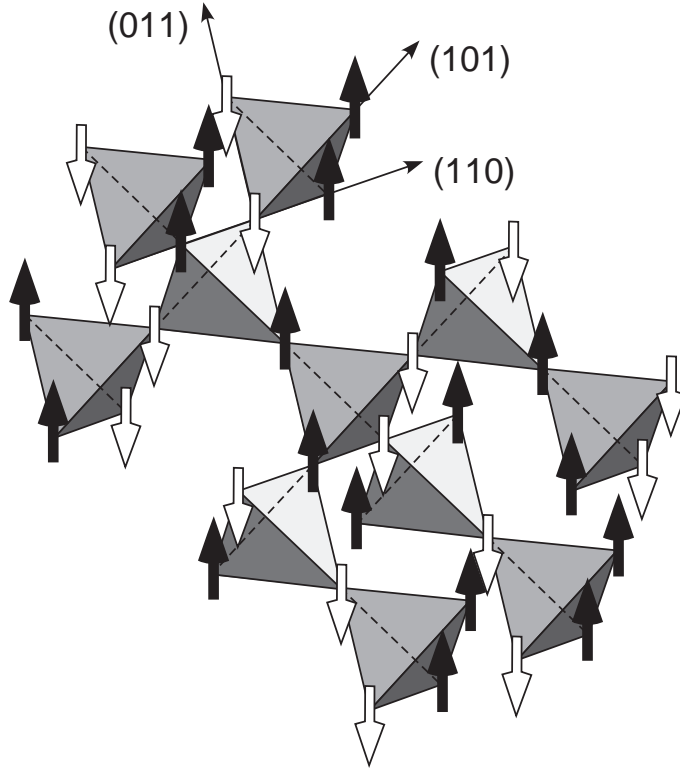
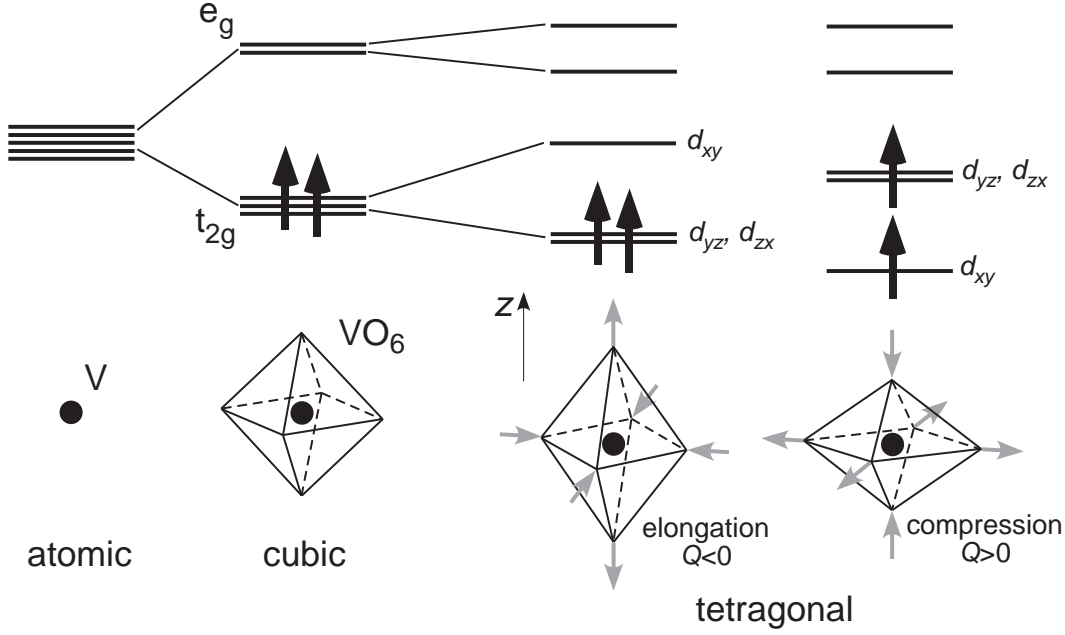


Fig. 2. Magnetic ordering structure in the lowest-temperature phase of vanadium spinels determined by neutron scattering experiment.⁹⁾

compounds show two successive transitions.⁶⁾ One is a structural transition at $\sim 50\text{K}$ and the lattice changes its symmetry. While the lattice symmetry is cubic above the transition temperature, it changes to tetragonal below the temperature, and the system is compressed along one of the principal axes, the c axis. The other transition takes place at a lower temperature $\sim 40\text{K}$, and ascribed to an antiferromagnetic ordering. The magnetic structure in the lowest-temperature phase was determined by neutron scattering experiment as shown in Fig. 2.⁹⁾ It consists of up-down-up-down- staggered antiferromagnetic pattern along the chains in the xy planes [(110) and $(1\bar{1}0)$ directions] and up-up-down-down- pattern with period four along the chains in the yz and zx planes [(101), $(10\bar{1})$, (011) and $(01\bar{1})$ directions]. Thus the fundamental questions are (i) what the driving mechanism of these successive transitions is and (ii) how the complicated magnetic ordering is stabilized. We will answer these questions theoretically by investigating keen competitions among spin, orbital and lattice degrees of freedom in this geometrically-frustrated system.

This paper is organized as follows. In Sec. 2, we examine a model with the Jahn-Teller coupling alone. We also examine a model with spin-orbital superexchange interaction alone in Sec. 3. In these two sections, we show that both two models fail to explain the experimental results. In Sec. 4, we take into account both two terms in the model and study keen competition between them. We show, by using

Fig. 3. Crystal-field splitting of d levels.

mean-field analysis and Monte Carlo simulation, that the model successfully explains two successive transitions of vanadium spinels. Effects of fluctuations, both thermal and quantum, are also discussed. In Sec. 5, we make some remarks on effects of relativistic spin-orbital coupling, direction of magnetic moment, and a possibility of Haldane gap state in this system. Section 6 is devoted to summary.

§2. Model with Jahn-Teller coupling

Let us start from a simple model with the Jahn-Teller coupling alone, which describes a coupling of orbital degrees of freedom with lattice distortions. In the octahedral position surrounded by a symmetric O_6 octahedron, the cubic crystal field splits the fivefold d levels of vanadium cation into higher twofold e_g levels and lower threefold t_{2g} levels (left two columns in Fig. 3). Jahn-Teller distortion is a distortion of O_6 octahedron, which gains energy by lifting the degeneracy further to achieve a closed-shell configuration of electronic state. In other words, the Jahn-Teller effect is active only for the case of an open-shell configuration, and hence, depends on the number of d electrons.

In vanadium spinels with divalent A -site cation AV_2O_4 , each vanadium has valence V^{3+} , and this corresponds to $(t_{2g})^2$ configuration. Hence, threefold t_{2g} levels are partially filled (second column in Fig. 3) so that the Jahn-Teller effect is active. We start from an ionic model describing independent VO_6 octahedra, and later we will introduce intersite correlations. If we consider the Jahn-Teller distortion of tetragonal symmetry, which is observed in experiments, the ionic model can be given

in the form

$$H_{\text{JT}}^{\text{ionic}} = \sum_i \gamma Q_i (n_{i1} + n_{i2} - 2n_{i3}) + \frac{1}{2} \sum_i Q_i^2, \quad (2.1)$$

where γ is the electron–phonon coupling constant and Q_i denotes the amplitude of local lattice distortion at site i . Here, we consider the tetragonal distortion along one of the principal axes, the z direction, and choose the sign of Q_i such that it is positive for a compression of the octahedron in the z direction. The orbital indices $\alpha = 1, 2$ and 3 of the density operator $n_{i\alpha}$ denotes d_{yz}, d_{zx} and d_{xy} , respectively. Assuming high–spin states by strong Hund’s–rule coupling, the model is defined for spinless fermions. The second term describes the elastic energy (Q is normalized to absorb the elastic constant); here we use the adiabatic approximation and phonons are regarded as classical objects. The model (2.1) is considered with the local constraint on the density as

$$\sum_{\alpha} \langle n_{i\alpha} \rangle = 2. \quad (2.2)$$

The ground state of the ionic model (2.1) is obtained by minimizing the energy under the constraint (2.2). The ground–state energy per site is given by

$$E_{\text{JT}}^{\text{ionic}} = -2\gamma^2 \quad \text{for } Q_i = -2\gamma, \quad (2.3)$$

and for the orbital states

$$\langle n_{i1} \rangle = \langle n_{i2} \rangle = 1 \quad \text{and} \quad \langle n_{i3} \rangle = 0. \quad (2.4)$$

This situation corresponds to the elongation of VO_6 octahedra as shown in the third column in Fig. 3: The doublet of d_{yz} and d_{zx} levels is lowered and occupied by two electrons to form the closed–shell configuration.

Experimentally, lattice distortion occurs in the opposite way at low temperatures, that is, a uniform compression of octahedra. If we restrict to the case of compression $Q > 0$, the energy minimum is found as

$$\tilde{E}_{\text{JT}}^{\text{ionic}} = -\frac{\gamma^2}{2} \quad \text{for } Q_i = \gamma, \quad (2.5)$$

and for the orbital states

$$\langle n_{i1} + n_{i2} \rangle = 1 \quad \text{and} \quad \langle n_{i3} \rangle = 1, \quad (2.6)$$

which are shown in the last column in Fig. 3.

In the real lattice structure, the Jahn–Teller effect should have some cooperative aspect — VO_6 octahedra share oxygen ions between neighbors, which leads to inter-site correlations of the Jahn–Teller distortion. Since spinel lattice structure consists of three–dimensional network of edge–sharing octahedra as shown in Fig. 4, a distortion of VO_6 octahedron tends to distort neighboring octahedra in the same manner. In other words, a ferro–type correlation is expected for the tetragonal distortions between neighboring octahedra. This tendency is mimicked by the ferro–type intersite coupling of the distortion as

$$H_{\text{JT}}^{\text{nn}} = -\lambda \sum_{\langle ij \rangle} Q_i Q_j, \quad (2.7)$$

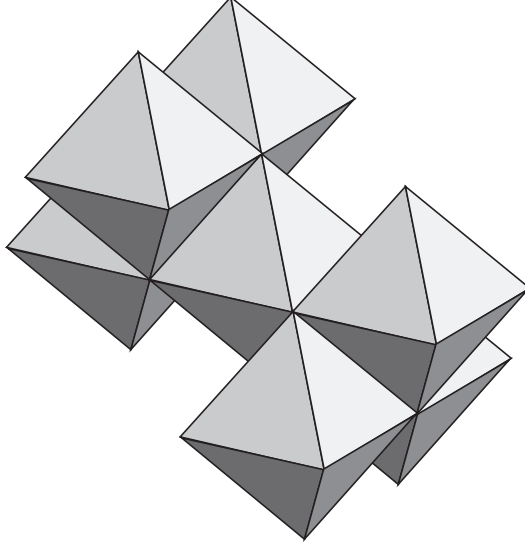


Fig. 4. Edge-sharing network of VO_6 octahedra in the spinel structure. Vanadium cations locate in the center of each octahedron and constitute the pyrochlore lattice in Fig. 1.

where $\lambda > 0$ is the coupling constant and the summation is taken over the nearest-neighbor sites on the pyrochlore lattice which consists of vanadium cations.

If we omit farther-neighbor correlations beyond the nearest neighbors, the total Hamiltonian for the Jahn–Teller effect is given by

$$H_{\text{JT}} = H_{\text{JT}}^{\text{ionic}} + H_{\text{JT}}^{\text{nn}}. \quad (2.8)$$

We can minimize the total energy with respect to Q_i by assuming uniform orbital states at all sites. This corresponds to find a mean-field solution for cooperative Jahn–Teller distortion of ferro-type, which is naturally expected for the ferro-type intersite coupling in Eq. (2.7). For the orbital state (2.4), or equivalently for an elongation of all VO_6 octahedra, we obtain the minimum of energy per site as

$$E_{\text{JT}} = -\frac{2\gamma^2}{1-6\lambda} \quad \text{for } Q_i = -\frac{2\gamma}{1-6\lambda}. \quad (2.9)$$

Note that $0 < \lambda < 1/6$ is required to keep the system stable. On the other hand, for the orbital state (2.6), corresponding to a compression of octahedra, we find a minimum as

$$\tilde{E}_{\text{JT}} = -\frac{\gamma^2}{2(1-6\lambda)} \quad \text{for } Q_i = \frac{\gamma}{1-6\lambda}. \quad (2.10)$$

Since $E_{\text{JT}} < \tilde{E}_{\text{JT}}$, the model with Jahn–Teller effect alone predicts a uniform elongation of all VO_6 octahedra, which apparently disagrees with the experimental result. In order to stabilize the compression of octahedra as observed in experiments, we need to compensate the energy difference per site

$$\Delta_{\text{JT}} = \tilde{E}_{\text{JT}} - E_{\text{JT}} = \frac{3\gamma^2}{2(1-6\lambda)} \quad (2.11)$$

by some energy gain from other mechanisms. We will see in Sec. 4 that this compensation indeed comes from the orbital superexchange interaction.

§3. Model with superexchange interaction

3.1. Model Hamiltonian

Next we examine effects of spin and orbital superexchange interactions. The superexchange interactions describe effective intersite couplings of both spin and orbital degrees of freedom in low-energy physics of strongly-correlated insulators. They are derived from a multi-orbital Hubbard model by using the perturbation in the strong-correlation limit.

We start from the Hubbard model with threefold orbital degeneracy corresponding to the t_{2g} manifold. The Hamiltonian reads

$$H_{\text{Hub}} = \sum_{ij} \sum_{\alpha\beta} \sum_{\tau} (t_{i\alpha,j\beta} c_{i\alpha\tau}^\dagger c_{j\beta\tau} + \text{H.c.}) + \frac{1}{2} \sum_i \sum_{\alpha\beta,\alpha'\beta'} \sum_{\tau\tau'} U_{\alpha\beta,\alpha'\beta'} c_{i\alpha\tau}^\dagger c_{i\beta\tau'}^\dagger c_{i\beta'\tau'} c_{i\alpha'\tau}, \quad (3.1)$$

where i, j and τ, τ' are site and spin indices, respectively, and $\alpha, \beta = 1$ (d_{yz}), 2 (d_{zx}), 3 (d_{xy}) are orbital indices. The first term of H_{Hub} is the electron hopping, and the second term describes onsite Coulomb interactions, for which we use the standard parametrizations,

$$U_{\alpha\beta,\alpha'\beta'} = U' \delta_{\alpha\alpha'} \delta_{\beta\beta'} + J_{\text{H}} (\delta_{\alpha\beta'} \delta_{\beta\alpha'} + \delta_{\alpha\beta} \delta_{\alpha'\beta'}), \quad (3.2)$$

$$U = U' + 2J_{\text{H}}. \quad (3.3)$$

In order to describe the low-energy effective theory for the insulating state of vanadium spinels, we apply the second-order perturbation in the hopping term. The unperturbed states are atomic eigenstates with two electrons on each vanadium cations in a high-spin state ($S = 1$). Among various hopping processes, the most relevant contribution is the nearest-neighbor σ bond, because the spinel lattice structure consists of three-dimensional network of edge-sharing VO_6 octahedra in Fig. 4.^{10,11)} This is the hopping in the case where one of four lobes of each t_{2g} orbital is pointing towards the other end of the bond. In the perturbation, we take account of this σ -bond contribution only for simplicity. The superexchange Hamiltonian, which is called the Kugel-Khomskii type Hamiltonian,¹²⁾ is obtained for the nearest-neighbor sites in the form

$$H_{\text{SE}}^{\text{nn}} = -J \sum_{\langle ij \rangle} [h_{\text{o-AF}}^{(ij)} + h_{\text{o-F}}^{(ij)}], \quad (3.4)$$

$$h_{\text{o-AF}}^{(ij)} = (A + B \mathbf{S}_i \cdot \mathbf{S}_j) [n_{i\alpha(ij)}(1 - n_{j\alpha(ij)}) + (1 - n_{i\alpha(ij)})n_{j\alpha(ij)}], \quad (3.5)$$

$$h_{\text{o-F}}^{(ij)} = C(1 - \mathbf{S}_i \cdot \mathbf{S}_j) n_{i\alpha(ij)} n_{j\alpha(ij)}, \quad (3.6)$$

where \mathbf{S}_i is the $S = 1$ spin operator and $n_{i\alpha} = \sum_{\tau} c_{i\alpha\tau}^\dagger c_{i\alpha\tau}$ is the density operator for site i and orbital α . Here, $\alpha(ij)$ is the orbital which has a finite hopping integral

between the sites i and j , for instance, $\alpha(ij) = 3$ (d_{xy}) for i and j sites in the same xy plane. Parameters in Eqs. (3.4)–(3.6) are given by coupling constants in Eq. (3.1) as

$$J = \frac{(t_{\sigma}^{\text{nn}})^2}{U}, \quad (3.7)$$

$$A = \frac{1 - \eta}{1 - 3\eta}, \quad B = \frac{\eta}{1 - 3\eta}, \quad C = \frac{1 + \eta}{1 + 2\eta}, \quad (3.8)$$

where t_{σ}^{nn} is the hopping integral of σ bond, and $\eta = J_{\text{H}}/U$ is a small parameter of ~ 0.1 . Note that each site is subject to the local constraint, $\sum_{\alpha=1}^3 n_{i\alpha} = 2$.

The superexchange model (3.4) consists of two contributions, $h_{\text{o-AF}}^{(ij)}$ and $h_{\text{o-F}}^{(ij)}$: The former favors spin-ferro and orbital-antiferro configuration on ij bond while the latter favors spin-antiferro and orbital-ferro configuration. The competition between these two exclusive contributions is a general aspect of Kugel–Khomskii type models. Another characteristic feature is the difference in the symmetry of the interactions. In the spin sector, the superexchange coupling is $\mathbf{S}_i \cdot \mathbf{S}_j$, isotropic Heisenberg type and independent of the bond direction. On the other hand, the superexchange coupling in the orbital sector becomes anisotropic because transfer integrals depend on orbital indices as well as the bond direction. Particularly in the present model (3.4), the anisotropy is conspicuous. The orbital exchange interaction depends only on the density operator, in other words, it is a three-state clock type interaction — there is no quantum fluctuation because the density operator is a constant of motion. Moreover, the orbital interaction depends on the bond direction and the orbital states in two sites in a complicated way. These features come from the dominant role of transfer integrals of σ bond, which are orbital diagonal and strongly depend on the bond direction and the orbital states.

3.2. Ground state

Now we examine the ground state of the superexchange Hamiltonian (3.4) defined on the pyrochlore lattice. Here, we consider the ground state with four-sublattice ordering in V_4 tetrahedron unit cell. Let us suppose $\eta = 0$ for a while. In this case, the energy is minimized for two different spin-orbital configurations in Fig. 5: The energy per site is $E_{\text{SE}} = -4J$, with counting the interactions with neighboring tetrahedra. Per tetrahedron unit cell, the configuration (a) contains four spin-antiferro orbital-ferro bonds (the energy is $-2J$ per bond), four spin-antiferro orbital-antiferro bonds ($-J$), and four spin-ferro orbital-antiferro bonds ($-J$). The configuration (b) contains four spin-antiferro orbital-ferro bonds, two spin-antiferro orbital-antiferro bonds, and six spin-ferro orbital-antiferro bonds.

The degeneracy between these two states is lifted for $\eta > 0$. Energies per site for configuration (a) and (b) are given by

$$E_{\text{SE}}^{(\text{a})} = -2J(A + C), \quad E_{\text{SE}}^{(\text{b})} = -2J(A + \frac{1}{2}B + C), \quad (3.9)$$

respectively. Since B is positive, the configuration (b) has a lower energy. This appears to be inconsistent with experiments: The spin structure in (b) is incompatible with the antiferromagnetic state observed in experiments in Fig. 2 because two

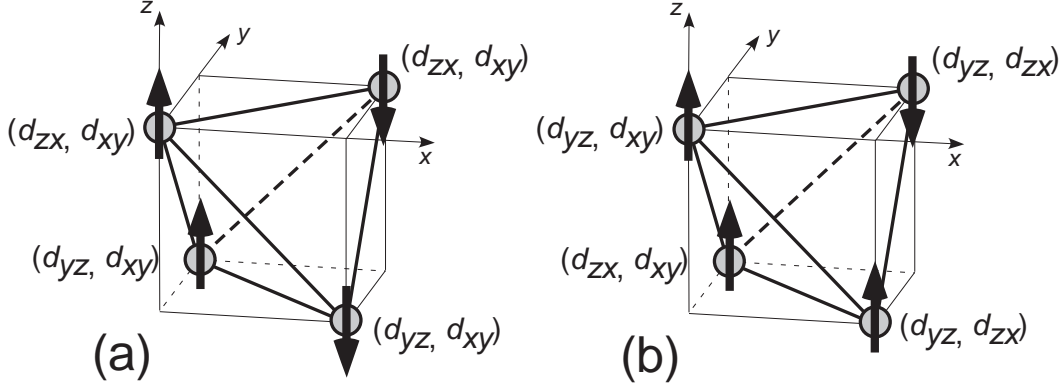


Fig. 5. Candidates for the ground states with four-sublattice ordering of the superexchange model (3·4). Spin and orbital configurations in tetrahedron unit cell are shown. Arrows denote spins, and labels (d_{yz}, d_{xy}) , etc., indicate two occupied orbitals at each site.

neighboring spins in the lower xy plane are parallel whereas the experimental spin configuration is antiparallel in all xy planes. Moreover, configuration (b) noticeably breaks the tetragonal symmetry which is experimentally observed in structurally-ordered phase. Hence, this mean-field type analysis for the ground state tells that the model with superexchange interactions alone fails to reproduce the experimental results.¹³⁾

There is, however, one caveat — the energy difference between the ground state (b) and the next lowest state (a) is small compared to the relevant energy scale in experiments. The energy difference between (a) and (b) per site is given by

$$\Delta_{SE} = E_{SE}^{(a)} - E_{SE}^{(b)} = JB = \frac{J\eta}{1 - 3\eta}. \quad (3\cdot10)$$

Let us roughly estimate this energy difference. As discussed in Ref. 2), estimates for vanadium spinels are $J \sim 200\text{K}$ and $\eta \sim 0.1$. Hence, the energy difference becomes $\Delta_{SE} \sim 30\text{K}$, which is smaller than the structural transition temperature $\sim 50\text{K}$. This strongly suggests that spin and orbital configuration in the ground state is sensitive to competing interactions; in particular, the stable configuration may be changed by including the cooperative Jahn–Teller effect, which apparently plays an important role in the structural transition. Indeed, we will see that the energy for the state (a) can be lower than for (b) in some parameter regime of the Jahn–Teller coupling — see Sec. 4.

3.3. Instability from high-temperature phase

We can gain further insight into the stable spin and orbital configuration of the model (3·4) by using another mean-field type argument. We here discuss fluctuation effects and an instability in spin and orbital sectors when we decrease temperature from high-temperature phase.¹⁾

Let us first examine the fluctuations in the spin sector. For this purpose, we replace the density operators in the orbital part of model (3·4) by their expectation

values in the high-temperature regime; $n_{i\alpha} \rightarrow \langle n_{i\alpha} \rangle = 2/3$. Then we end up with the reduced Hamiltonian describing the spin sector only, which reads

$$H_{\text{spin}}^{\text{nn}} = J_S \sum_{\langle ij \rangle} \mathbf{S}_i \cdot \mathbf{S}_j, \quad (3.11)$$

up to irrelevant constants, where the effective exchange constant is given by

$$J_S = \frac{4}{9}J(C - B). \quad (3.12)$$

Since J_S is positive for small $\eta \sim 0.1$, the reduced model (3.11) is the antiferromagnetic Heisenberg model with $S = 1$ spins defined on the pyrochlore lattice. It is known that the spin correlations hardly develop in this model because of the strong geometrical frustration. A possibility of a valence-bond-solid type ordering with the aid of spin-lattice coupling has been discussed,¹⁴⁾ however it is not easy to explain two successive transitions in vanadium spinels by this spin Jahn-Teller scenario. The present consideration implies that the magnetic instability cannot occur in the high-temperature orbital-para phase.

Next we consider the instability in the orbital sector. In this case, we replace the spin part of model (3.4) by their mean value in high-temperature regime, that is, $\mathbf{S}_i \rightarrow \langle \mathbf{S}_i \rangle = 0$. The resultant Hamiltonian for the orbital degree of freedom reads

$$H_{\text{orbital}}^{\text{nn}} = J_O \sum_{\langle ij \rangle} n_{i\alpha(ij)} n_{j\alpha(ij)}, \quad (3.13)$$

up to irrelevant constants, where

$$J_O = J(2A - C). \quad (3.14)$$

This coupling constant J_O is also positive so that Eq. (3.13) is also the antiferro-type model on the pyrochlore lattice as the model (3.11). A crucial difference between the two models is the form of interactions: The orbital model (3.13) has anisotropic interaction (three-state clock type) which strongly depends on the bond direction and the orbital states. This peculiar form of the orbital coupling lifts the degeneracy in this pyrochlore system, at least partially — the three-state clock model still suffers from a frustration on the pyrochlore lattice. The lowest energy is achieved by four orbital-antiferro bonds and two orbital-ferro bonds within each tetrahedron. There are two different types of orbital configurations with these bonds as shown in Fig. 6: In type (a), two orbital-ferro bonds do not touch with each other, while they touch at one corner of the tetrahedron in type (b). Note that these orbital configurations coincide with those in Fig. 5. The energy of the reduced orbital model (3.13) is the same for these two configurations. Hence, there remains degeneracy in the orbital sector although the degeneracy is reduced and not severe compared to that in the spin sector in the model (3.11).

The degeneracy remaining in the orbital sector is easily lifted by including the Jahn-Teller effects. This will be discussed in Sec. 4.

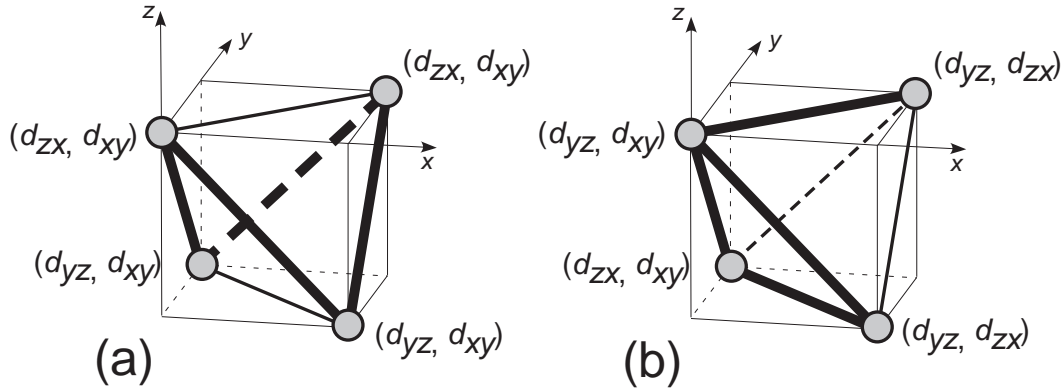


Fig. 6. Stable orbital configurations of the effective orbital model (3.13). Labels (d_{yz}, d_{xy}) , etc., indicate two occupied orbitals at each site. Thick lines denote orbital-antiferro bonds.

§4. Model with both superexchange and Jahn–Teller couplings

In this section, we examine the model with both superexchange interactions and Jahn–Teller couplings. In Sec. 4.1, we will show how the mean-field arguments in Sec. 3 are modified by including Jahn–Teller distortions in addition to the superexchange model. We will point out that once both superexchange and Jahn–Teller effects are taken into account, the degeneracy in the orbital sector is lifted and an orbital ordering takes place. We will also show that spin frustration partially remains in the presence of the orbital ordering, which is finally reduced by farther-neighbor exchange couplings. In Sec. 4.2, the mean-field picture is examined and confirmed by Monte Carlo simulation. Thermodynamic properties are compared with experimental results. In Sec. 4.3, effect of quantum fluctuations, which is neglected in both mean-field argument and Monte Carlo simulation, is examined by using linearized spin-wave theory.

4.1. Mean-field type analysis

We have shown in Sec. 3 that the Kugel–Khomskii type of spin-orbital model has two competing stable states for V_4 tetrahedron unit. For realistic values of parameters for the vanadium spinel, it was found that the lowest-energy state has a different symmetry from the experimental results and is not compatible with the antiferromagnetic order in experiments. This does not imply the failure of the Kugel–Khomskii model but that one needs to take account of couplings to lattice distortion.

Below the structural transition temperature at $\sim 50\text{K}$, the lattice shows a tetragonal distortion, and VO_6 octahedra are uniformly compressed along the c axis ($c < a$). Energy level scheme in this case is shown at right most in Fig. 1, and three degenerate t_{2g} orbitals in cubic crystal field are split to higher-energy doublet and lower-energy singlet states in tetragonal field:

$$e(d_{yz}) = e(d_{zx}) = e(t_{2g}) + \frac{\Delta}{3}, \quad e(d_{xy}) = e(t_{2g}) - \frac{2}{3}\Delta. \quad (4.1)$$

As shown in Eq. (2.1), the level splitting $\Delta = e(d_{yz,zx}) - e(d_{xy})$ is proportional to

the tetragonal distortion, $\Delta = 3\gamma Q$ with $Q \propto 1 - c/a$.

Let us first reanalyze stable orbital configuration in spin paramagnetic phase with taking account of the Jahn–Teller effects. We showed in Sec. 3.3 that two types of orbital configurations in Fig. 6 have the same energy of the effective orbital interaction (3.12). Configuration (a) is compatible with the tetragonal symmetry as that of the intermediate–temperature phase experimentally observed below the structure transition temperature, whereas configuration (b) has a lower symmetry. Energy gain due to the Jahn–Teller effects is largest when the lattice is compressed along the z axis for configuration (a) but along the x or y axis for configuration (b). The corresponding energies per site are respectively,

$$E_{\text{JT}}^{(\text{a})} = -\frac{\Delta}{3}, \quad E_{\text{JT}}^{(\text{b})} = -\frac{\Delta}{12}. \quad (4.2)$$

Therefore, the tetragonal orbital configuration (a) has a lower energy and is stabilized by the Jahn–Teller effects, as far as a uniform mode of distortion is considered.

Next, let us reexamine the stability at $T = 0$, discussed in Sec. 3.2, by including the effects of tetragonal lattice distortions. The energy gain of the configuration is largest when the lattice is compressed in the same matter as for the previous orbital model. The configurations shown in Fig. 2 (a) and (b) have energies, respectively,

$$E_{\text{SE+JT}}^{(\text{a})} = E_{\text{SE}}^{(\text{a})} + E_{\text{JT}}^{(\text{a})} = -2J(A + C) - \frac{\Delta}{3}, \quad (4.3)$$

$$E_{\text{SE+JT}}^{(\text{b})} = E_{\text{SE}}^{(\text{b})} + E_{\text{JT}}^{(\text{b})} = -2J(A + \frac{1}{2}B + C) - \frac{\Delta}{12}, \quad (4.4)$$

where $E_{\text{SE}}^{(\text{a}),(\text{b})}$ are given in Eq. (3.9). Comparing these two, one finds that the configuration (a) has a lower energy than (b) when

$$\Delta > 4JB = \frac{4J\eta}{1 - 3\eta}. \quad (4.5)$$

As was emphasized in previous sections, the vanadium spinels are the system in which the Jahn–Teller couplings compete with the spin–orbital interactions, $\Delta \sim J \times (\text{coordination number})$. Recalling that η is small, we may expect that the above condition is satisfied and that the configuration (a) with tetragonal symmetry is most stable, if spin–orbital superexchange interactions and Jahn–Teller couplings are both considered. In Sec. 4.2, we will demonstrate by Monte Carlo calculations that the tetragonal orbital order (a) actually appears at finite temperatures.

Next, let us discuss the spin configuration in the magnetic phase. The configuration in Fig. 5(a) imposes the spin configuration inside the tetrahedron unit cell, and one needs to consider correlations between different tetrahedra. The spin order at $\sim 40\text{K}$ was observed by neutron scattering experiment⁹⁾ and the determined spin pattern is shown in Fig. 2. This pattern corresponds to the $\mathbf{Q} = (0, 0, 2\pi/c)$ order of the configuration in Fig. 5(a) (c is the length of cubic unit cell along the z axis), i.e., uniform packing in the xy planes and alternate stacking in the z direction with spin inversion from layer to layer. Antiferromagnetic spin pattern along chains in the xy planes are easily explained, since any pair of nearest–neighbor spins in xy

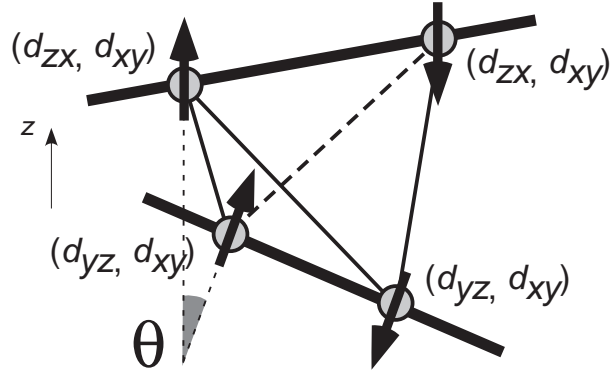


Fig. 7. Frustration between neighboring xy chains remaining in the mean-field level. The mean-field energy does not depend on the relative angle θ between the antiferromagnetic chains.

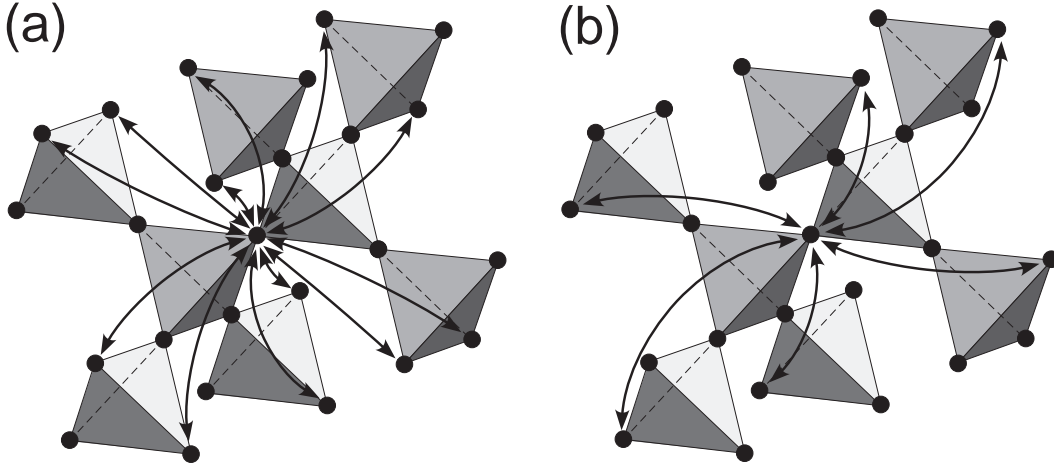


Fig. 8. (a) Second-neighbor exchange couplings, and (b) third-neighbor exchange couplings.

chains should be anti-parallel. However, there are no correlations between different xy chains within the level of the mean-field approximation. Look the spin configuration in Fig. 5(a) and rotate two spins in the lower xy plane with imposing that they are always anti-parallel to each other as in Fig. 7. Such rotations do not change the energy in the mean-field level, and this implies no correlation between two chains. This is due to the frustrated lattice structure and antiferromagnetic nearest-neighbor correlations in each chain.

Since interchain correlations are not determined by nearest-neighbor couplings, we have to consider the effects of longer-range couplings, which are much weaker in amplitude than the nearest-neighbor ones and are usually neglected. These longer-range couplings are shown in Fig. 8. Another possible mechanism is order by disorder.¹⁵⁾ However, as we will discuss later based on numerical (Sec. 4.2) and analytical (Sec. 4.3) calculations, the mechanism of order by disorder is not sufficient to explain a finite static moment in the magnetic phase. As shown in Fig. 9, once antiferromagnetic correlations develop in the xy chains, it is important to note that

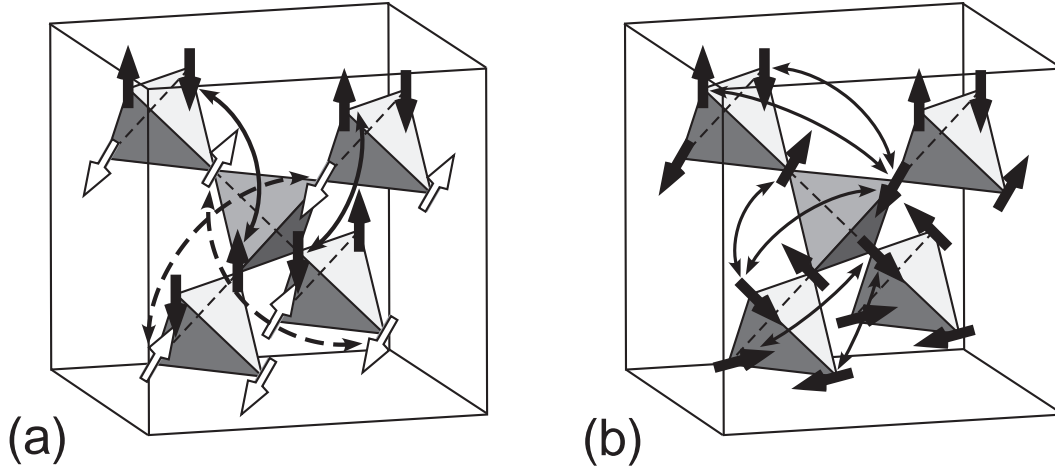


Fig. 9. (a) Two sets of spin chains coupled by third-neighbor exchange couplings J_3 are depicted in black and white colors. (b) Second-neighbor coupling J_2 are strongly frustrated between neighboring antiferromagnetic chains in the xy planes.

third-neighbor couplings lead to more dominant effects than second-neighbor ones. Third-neighbor couplings connect antiferromagnetic chains every two xy planes as shown in Fig. 9(a). As a consequence, the whole system becomes two interpenetrating sets of three-dimensional spin system [black and white spins in Fig. 9(a), respectively]. These two sets are connected by nearest-neighbor and second-neighbor couplings. However, their mean fields are canceled out and lead to no effects. The frustration of second-neighbor exchanges is depicted in Fig. 9(b). In this case, it is fluctuations which determine the correlation between the two sets. We discussed the effects of quantum fluctuations, in particular, in Ref. 1), and it was found that the collinear spin order is stabilized. Monte Carlo results in the next section show that thermal fluctuations also stabilize the same collinear order.

4.2. Monte Carlo study

Now we investigate the thermodynamic properties of the model with both superexchange interaction and Jahn–Teller coupling by using Monte Carlo method. In Sec. 4.2.1, we briefly describe the Monte Carlo technique and the model parameters used in the simulation. In Sec. 4.2.2, the model with nearest-neighbor couplings is studied. We will show that the orbital ordering takes place at a finite temperature but the magnetic frustration remains down to the lowest temperature. Effects of third-neighbor exchange interactions will be examined in Sec. 4.2.3. As predicted in the mean-field argument, Monte Carlo results show that the magnetic frustration is reduced and antiferromagnetic order is stabilized at a finite temperature. The phase diagram by controlling the third-neighbor coupling will be shown in Sec. 4.2.4.

4.2.1. Method and parameters

In order to investigate thermodynamic properties of the effective spin–orbital–lattice coupled model, we use Monte Carlo calculations. Quantum Monte Carlo

simulation is known to be difficult for frustrated models because of the negative sign problem. In the present study, we neglect quantum fluctuations and approximate the model in the classical level. This approximation retains effects of thermal fluctuations that may play dominant roles in finite-temperature transitions. The quantum nature originates only from spin $S = 1$ operators because the orbital interaction in Eq. (3.4) is classical, and because Jahn–Teller lattice distortions are treated as classical variables in Eq. (2.8). We approximate the spin operators by classical vectors with the modulus $|\mathbf{S}| = 1$ to give largest z component $S_z = 1$ in the classical part. Therefore, our model for Monte Carlo simulation consists of the classical Heisenberg part in the spin sector, the three-state clock part in the orbital sector, and the classical phonon part.

We use a standard metropolis algorithm with local updates. We typically perform 10^5 Monte Carlo samplings for measurements after 10^5 steps for equilibration. The system sizes in the present work are up to $L = 12$, where L is the linear dimension of the system measured in the cubic units, i.e., the total number of sites N_{site} is up to $12^3 \times 16 = 27648$. We set $J = 1$ as an energy unit and the lattice constant of cubic unit cell as a length unit. We use the convention of the Boltzmann constant $k_B = 1$. The following results are for $\eta = 0.08$, $\gamma^2 = 0.04$ and $\lambda = 0.15$. Readers are referred to Ref. 2) for more details of Monte Carlo simulation.

4.2.2. Model with nearest-neighbor couplings only

Let us first examine what happens in the model with the nearest-neighbor interactions only, whose Hamiltonian consists of the nearest-neighbor superexchange interactions (3.4) and the Jahn–Teller coupling (2.8);

$$H = H_{\text{SE}}^{\text{nn}} + H_{\text{JT}}. \quad (4.6)$$

The mean-field type analysis in Sec. 4.1 predicts that the orbital-ordered state in Fig. 6(a) is stabilized by a cooperative effect of orbital interaction and Jahn–Teller coupling, but spin frustration partially remains even in the presence of the orbital ordering. More precisely, the staggered antiferromagnetic correlation develops along the chains in the xy planes, however the coupling between the neighboring chains remains frustrated: Hence, the system cannot develop three-dimensional magnetic long-range order. We examine this mean-field picture by using Monte Carlo simulation.

Figure 10 shows the temperature dependence of the specific heat per site, which is calculated by fluctuations of the internal energy as

$$C = \frac{\langle H^2 \rangle - \langle H \rangle^2}{T^2 N_{\text{site}}}. \quad (4.7)$$

The brackets denote thermal averages by Monte Carlo sampling. The specific heat shows a jump at $T_O \simeq 0.23J$, indicating a first-order transition.

At this transition temperature, orbital ordering takes place. Figure 11 shows the sublattice orbital moment, which is calculated in the form

$$M_O = \frac{4}{N_{\text{site}}} \left\langle \left| \sum_{i \in \text{sublattice}} \mathbf{I}_i \right| \right\rangle, \quad (4.8)$$

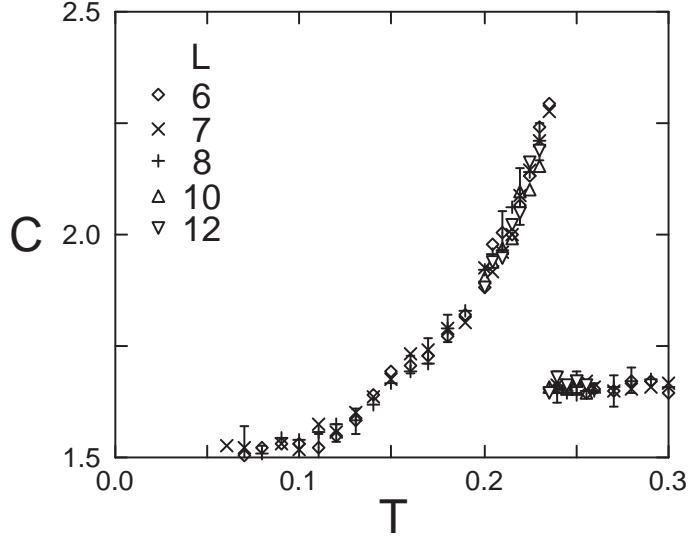


Fig. 10. Temperature dependence of the specific heat per site [Eq. (4.7)] for the model with nearest-neighbor interactions only.

where the summation is taken over the sites within one of the four sublattices in tetrahedron unit cell. Here, \mathbf{I}_i is the three-state clock vector at the site i which describes three different orbital states as shown in the inset of Fig. 11; $\mathbf{I}_i = (1, 0)$ for (d_{yz}, d_{xy}) , $\mathbf{I}_i = (-1/2, \sqrt{3}/2)$ for (d_{yz}, d_{zx}) , and $\mathbf{I}_i = (-1/2, -\sqrt{3}/2)$ for (d_{zx}, d_{xy}) orbital occupations, respectively. It is found that the values of M_O for four different sublattices have the same value within the error bars so that we omit the sublattice index in Eq. (4.8). As shown in Fig. 11, M_O shows a clear jump at $T_O \simeq 0.23J$ where the specific heat jumps. This indicates that a four-sublattice orbital ordering occurs at T_O .

Figure 12 plots the orbital distribution for four sublattices in tetrahedron unit cell, which is defined as

$$\bar{n}_\alpha = \frac{4}{N_{\text{site}}} \sum_{i \in \text{sublattice}} \langle n_{i\alpha} \rangle, \quad (4.9)$$

where $\alpha = 1$ (d_{yz}), 2 (d_{zx}), and 3 (d_{xy}). The results indicate that the orbital distributions suddenly change from equally distributed state $\bar{n}_\alpha \sim 2/3$ in the high-temperature para phase to almost polarized state $\bar{n}_\alpha \sim 0$ or 1 below T_O . In the orbital ordered phase, d_{yz} ($\alpha = 1$) and d_{xy} ($\alpha = 3$) orbitals are occupied in the sublattices 1 and 4, and d_{zx} ($\alpha = 2$) and d_{xy} ($\alpha = 3$) orbitals are occupied in the sublattices 2 and 3. This orbital ordering structure is consistent with the mean-field prediction shown in Fig. 6(a).

Accompanying the transition at T_O , a tetragonal lattice distortion occurs discontinuously. In Fig. 13, we plot the average of the Jahn-Teller distortions which is

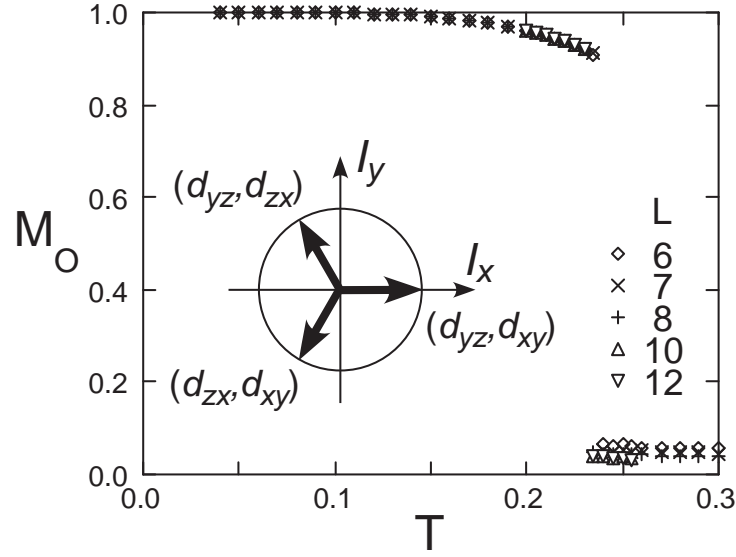


Fig. 11. The sublattice orbital moment in Eq. (4.8). The inset shows the three-state clock vector for the orbital state.

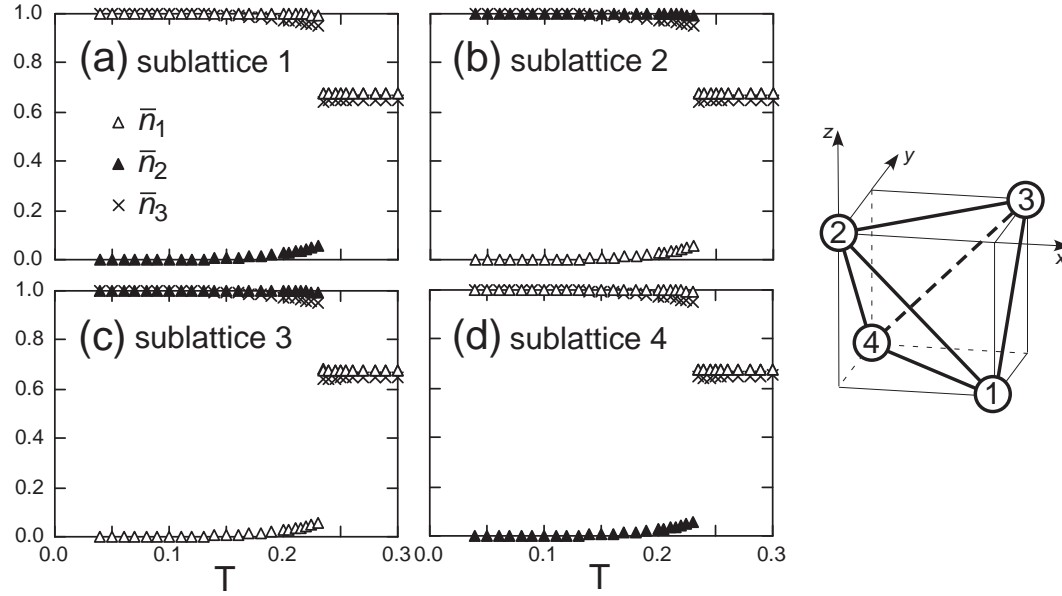


Fig. 12. Electron density in each orbital for four sublattices 1-4 defined in Eq. (4.9). The data are calculated at $L = 8$.

calculated by

$$\bar{Q} = \sum_i \frac{\langle Q_i \rangle}{N_{\text{site}}}. \quad (4.10)$$

The positive value of \bar{Q} below T_O corresponds to a ferro-type tetragonal distortion with a compression of VO_6 octahedra.

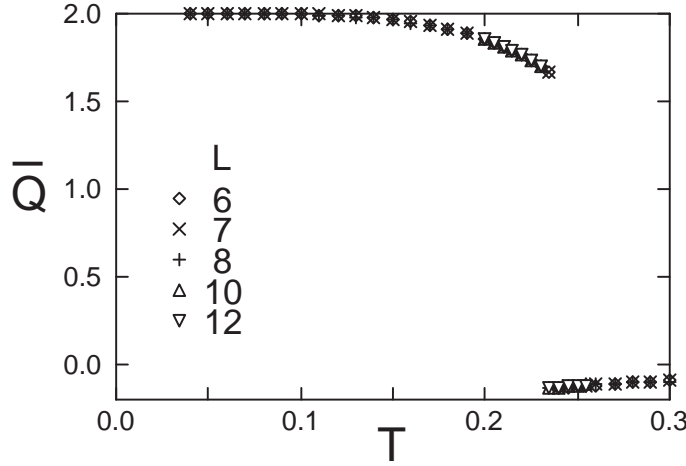


Fig. 13. The average of the Jahn–Teller distortion defined in Eq. (4·10).

Therefore, the discontinuous transition at $T_O \simeq 0.23J$ is ascribed to the orbital ordering with the tetragonal Jahn–Teller distortion. The orbital and lattice ordered state in the low–temperature phase is consistent with the mean–field prediction.

So much for the orbital and lattice state — what about the spin sector? Monte Carlo results clearly indicate that spin frustration remains even below T_O as predicted in the mean–field picture. Figure 14 plots temperature dependences of spin correlations for nearest–neighbor and third–neighbor pairs. The spin correlations are measured along the xy , yz and zx chains, respectively, as

$$S_{\text{nn}}^{(\nu)} = \sum_{\langle ij \rangle \in \nu} \frac{\langle \mathbf{S}_i \cdot \mathbf{S}_j \rangle}{N_b}, \quad S_{\text{3rd}}^{(\nu)} = \sum_{\langle\langle ij \rangle\rangle \in \nu} \frac{\langle \mathbf{S}_i \cdot \mathbf{S}_j \rangle}{N_b}, \quad (4.11)$$

where $\nu = xy, yz, zx$, and N_b is the number of the bonds in the summation. The summations with $\langle ij \rangle$ and $\langle\langle ij \rangle\rangle$ are for the nearest–neighbor sites and the third–neighbor sites along the ν chains, respectively.

As shown in Fig. 14(a), along the xy chains, the antiferromagnetic correlations develop below T_O . On the other hand, the spin correlations are strongly suppressed in the yz (and zx) directions as shown in Fig. 14(b). These results support the mean–field picture, which predicts the antiferromagnetic correlations along the xy chains and strong frustration between the chains. Since one–dimensional Heisenberg spin chain cannot order at any temperature because of strong fluctuations, the model (4·6), which includes only the nearest–neighbor couplings, does not show any magnetic ordering at finite temperature. This is the reason why we do not see any anomaly associated with magnetic ordering in the specific heat in Fig. 10.

4.2.3. Effect of third–neighbor superexchange interaction

The mean–field analysis in Sec. 4.1 predicts that the magnetic transition in experiments is reproduced by including third–neighbor superexchange interactions. Here, we examine this prediction by using Monte Carlo technique. Now the total

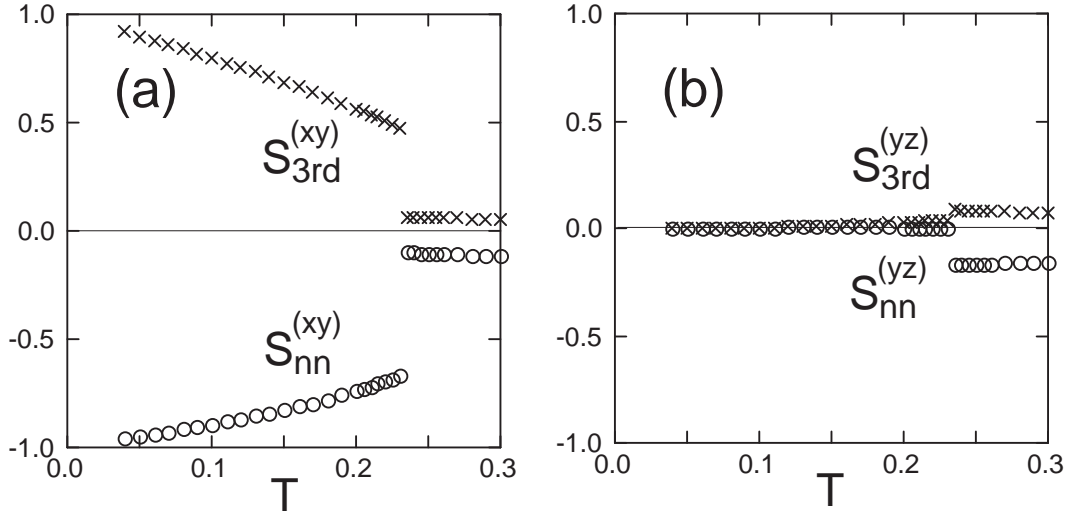


Fig. 14. Spin correlations for the nearest-neighbor sites and the third-neighbor sites defined by Eq. (4-11) along the (a) xy chains and (b) yz (or, equivalently zx) chains. The data are calculated for the model with nearest-neighbor interactions only with the system size $L = 8$.

Hamiltonian reads

$$H = H_{\text{SE}}^{\text{nn}} + H_{\text{SE}}^{\text{3rd}} + H_{\text{JT}}. \quad (4-12)$$

Here the third-neighbor superexchange term $H_{\text{SE}}^{\text{3rd}}$ is given by

$$H_{\text{SE}}^{\text{3rd}} = -J \sum_{\langle\langle ij \rangle\rangle} [h_{\text{o-AF}}^{(ij)} + h_{\text{o-F}}^{(ij)}], \quad (4-13)$$

where the summation is taken over the third-neighbor sites along the chains, and $h_{\text{o-AF}}^{(ij)}$ and $h_{\text{o-F}}^{(ij)}$ are given by Eqs. (3-5) and (3-6).

When we switch on the third-neighbor interaction J_3 , additional anomaly appears in the specific heat except for the jump associated with the orbital and lattice orderings. Figure 15 shows the specific heat per site at $J_3 = 0.02J$. In addition to the jump at $T_O \simeq 0.19J$, a peak appears at $T_N \simeq 0.115J$. This peak, not a jump, increases its height as the system size L , suggesting a divergence in the thermodynamic limit — a characteristic feature of a second-order phase transition.

The jump at $T_O \simeq 0.19J$ is ascribed to the discontinuous transition of orbital and lattice orderings. The order parameters behave in a similar manner as in Figs. 11 and 13 although the transition temperature T_O slightly decreases. On the other hand, the anomaly at $T_N \simeq 0.115J$ is ascribed to a magnetic ordering as explained in the following.

Figure 16 shows the spin correlations in Eq. (4-11) for the model (4-12) at $J_3 = 0.02J$. Compared to the results at $J_3 = 0$ in Fig. 14, a big difference is found in the third-neighbor spin correlation along the yz (and zx) chains; the antiferromagnetic correlation rapidly develops below $T_N \simeq 0.115J$. This suggests an emergence of three-dimensional magnetic ordering there.

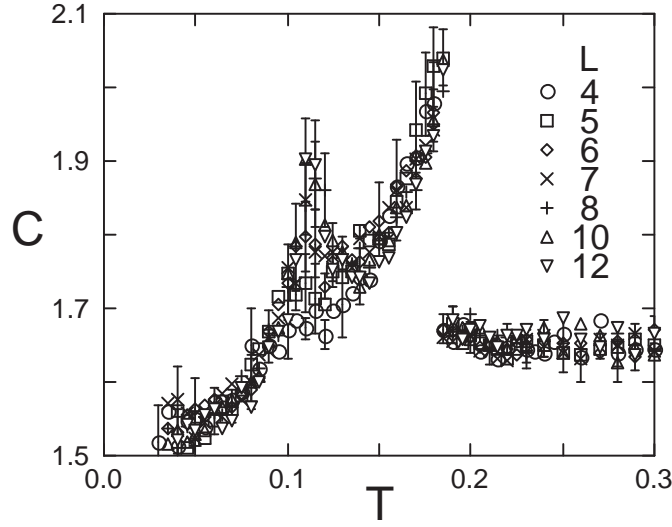


Fig. 15. Temperature dependence of the specific heat per site [Eq. (4.7)] for the model with the third-neighbor superexchange interaction $J_3 = 0.02J$.

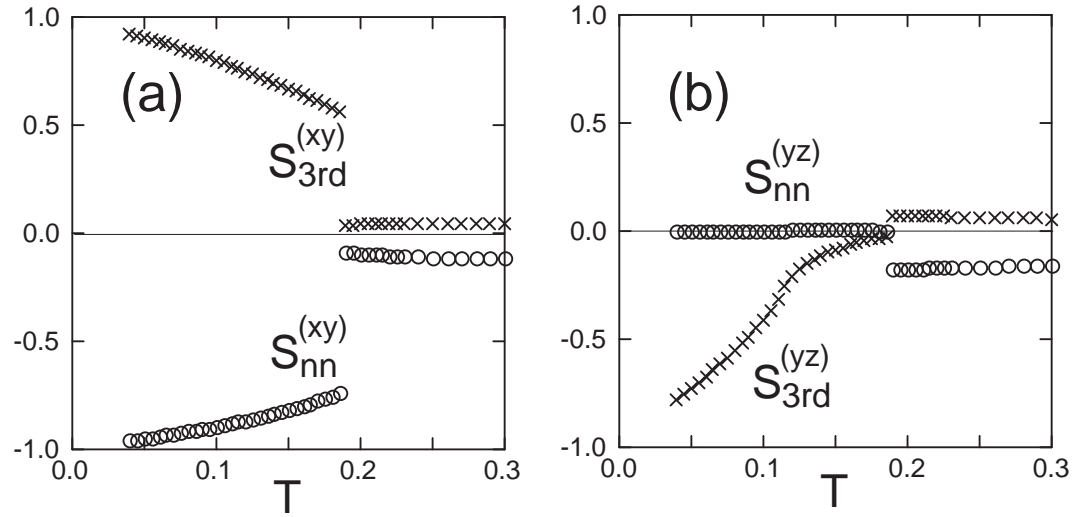


Fig. 16. Spin correlations [Eq. (4.11)] for $J_3 = 0.02J$. The data are calculated at $L = 12$.

We calculate the order parameters for the magnetic ordering. As described in Sec. 4.1, in the mean-field level, three-dimensional magnetic ordering takes place on two independent sublattices which consists of (110) chains and $(1\bar{1}0)$ chains, respectively [See Fig. 9(a)]. Here, we measure the staggered moment of these sublattice magnetizations, which is formally defined by

$$M_S = \left\langle \left| \frac{2}{N_{\text{site}}} \sum_i g_i \mathbf{S}_i \right|^2 \right\rangle^{\frac{1}{2}}, \quad (4.14)$$

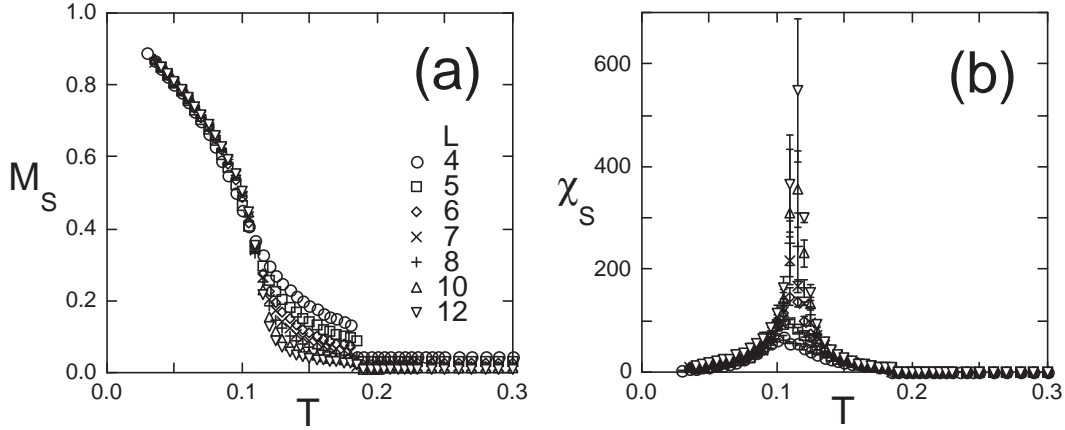


Fig. 17. (a) The staggered moment defined in Eq. (4.14). (b) The staggered magnetic susceptibility measured by fluctuations of M_S . The results are calculated at $J_3 = 0.02J$.

where the form factor g_i is given by

$$g_i = \cos[2\pi(x_i + y_i)] + i \cos[2\pi(x_i - y_i)]. \quad (4.15)$$

Here x_i and y_i are the x and y coordinates of the site i measured in the cubic unit, respectively. Note that g_i is specified only by the x and y coordinates of the site i because the z coordinate is uniquely determined within the cubic unit cell due to the special structure of the pyrochlore lattice.

Figure 17 plots the temperature dependences of the sublattice magnetization M_S in Eq. (4.14) and the corresponding susceptibility χ_S . As shown in Fig. 17(a), the staggered magnetization develops continuously below $T_N \simeq 0.115J$ and approaches the saturation moment $M_S = 1$ as $T \rightarrow 0$. The susceptibility shows a diverging behavior at T_N as shown in Fig. 17(b). These results indicate that the phase transition at T_N is a second-order one with the magnetic ordering of staggered sublattice moments.

In the mean-field level, two sublattice moments are independent. It is suggested that quantum fluctuations can align two moments and select a collinear magnetic ordering as discussed in Sec. 4.1. While the effect of quantum fluctuations is beyond our classical approach, our Monte Carlo study retains thermal fluctuations that are completely neglected in the mean-field argument, and it is known that in many frustrated systems thermal fluctuations also favor a collinear state.¹⁵⁾ Here we measure the collinearity between two sublattice moments \mathbf{M}_1 and \mathbf{M}_2 by

$$P = \frac{3}{2} \left[\left\langle \frac{(\mathbf{M}_1 \cdot \mathbf{M}_2)^2}{(\mathbf{M}_1)^2 (\mathbf{M}_2)^2} \right\rangle - \frac{1}{3} \right] = \frac{3}{2} \left[\langle \cos^2 \theta_{12} \rangle - \frac{1}{3} \right], \quad (4.16)$$

where θ_{12} is the angle between \mathbf{M}_1 and \mathbf{M}_2 . Note that P becomes 1 when the AF order is collinear, i.e., $\mathbf{M}_1 \parallel \mathbf{M}_2$, and that P becomes 0 when \mathbf{M}_1 and \mathbf{M}_2 are independent.

Figure 18 plots the measure of collinearity P . Below $T_N \simeq 0.115J$, P becomes finite and grows rapidly; it approaches 1 as the system size increases. This indicates

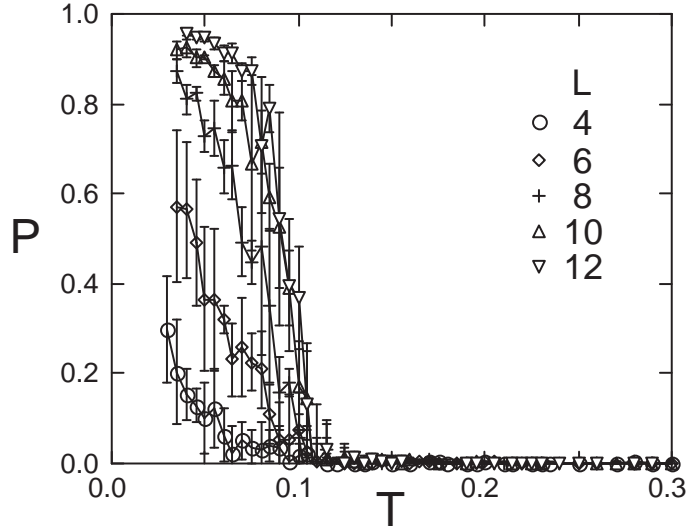


Fig. 18. The measure of collinearity defined in Eq. (4.16) at $J_3 = 0.02J$. The lines are guides for the eyes.

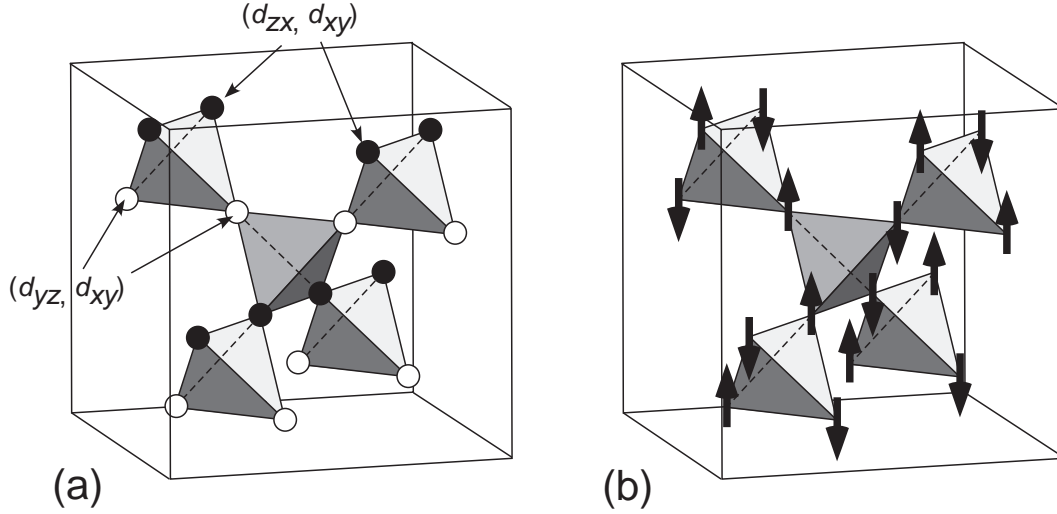


Fig. 19. Monte Carlo results for (a) orbital-ordering pattern and (b) spin-ordering pattern in the lowest-temperature phase. In (a), filled (open) circles denote the sites where d_{zx} and d_{xy} (d_{yz} and d_{xy}) orbitals are occupied.

that the magnetic state is collinear below T_N . Consequently, the magnetic order is indeed the same one observed in experiments, that is, up-down-up-down- staggered pattern along the xy chains and up-up-down-down- four-times period along the yz and zx chains — see Fig. 19(b).

Therefore, the present model (4.12), which includes the third-neighbor superexchange interactions, successfully explains the experimental results for both structural transition and antiferromagnetic transition. The structural transition at \sim

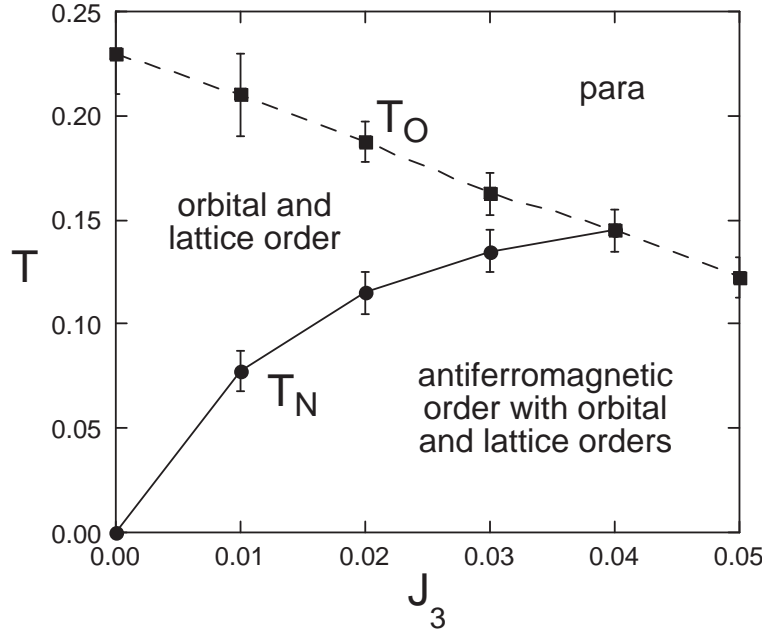


Fig. 20. Phase diagram for the spin-orbital-lattice coupled model determined by classical Monte Carlo calculations. The orbital and lattice transition at T_O (the dashed line) is a first-order transition, while the antiferromagnetic transition at T_N (the solid line) is a second-order one. The lines are guides for the eyes.

50K is understood as the orbital ordering accompanied by the tetragonal Jahn-Teller distortion of a compression of VO_6 octahedra. The orbital ordering pattern is a layered type — the so-called A-type order, which is alternative stacking of (d_{yz}, d_{xy}) -occupied layers and (d_{zx}, d_{xy}) -occupied layers in the z direction, as shown in Fig. 19(a). The transition at $\sim 40\text{K}$ is the antiferromagnetic transition. The transition temperature T_N is lower than T_O because the spin frustration is reduced. Below T_N , the complicated antiferromagnetic ordering appears as shown in Fig. 19(b), which is consistent with the neutron scattering result in Fig. 2. This magnetic ordering is stabilized by the third-neighbor superexchange J_3 as well as thermal fluctuations. The latter fluctuation effect is important to realize the collinear spin configurations by order-by-disorder mechanism.

4.2.4. phase diagram

The antiferromagnetic ordering is stabilized by J_3 , and hence, the transition temperature T_N increases as J_3 . On the other hand, the orbital and lattice transition temperature T_O slightly decreases as J_3 increases as found in previous sections. What happens for larger J_3 ?

We determined the phase diagram by changing J_3 . The result is shown in Fig. 20. The transition temperatures are determined by the specific heat, and the orbital, lattice and magnetic order parameters. As shown in Fig. 20, for large values of $J_3 > 0.03J$, T_N coincides with T_O , and there is only one discontinuous transition where both orbital and antiferromagnetic spin moments becomes finite discontinuously.

In the region of small J_3 , our model shows two transitions at different temperatures as observed in vanadium spinels. By using estimates of parameters $J \sim 200\text{K}$ and $J_3 \sim 0.02J \sim 4\text{K}$,²⁾ the transition temperatures in our results are $T_O \sim 40\text{K}$ and $T_N \sim 20\text{K}$. The experimental values are $\sim 50\text{K}$ and $\sim 40\text{K}$, respectively, in ZnV_2O_4 . The semiquantitative agreement of the transition temperatures is satisfactory.

4.3. Effects of quantum fluctuations

We have determined the ordering pattern of spin configuration based on the spin-orbital-lattice model and shown that it is consistent with the experimental result of elastic neutron scattering. The size of the static magnetic moment, however, needs further consideration, since it is subject to fluctuations and renormalized to a smaller value. To compare with the value at low temperatures in experiment, we now show that quantum fluctuations are very large in frustrated pyrochlore lattice, particularly when the third-neighbor exchange coupling J_3 is small, and the reduction of the moment is prominent.

Let us consider the Heisenberg model,

$$H_{\text{spin}} = \sum_{\langle ij \rangle} J_{ij} \mathbf{S}_i \cdot \mathbf{S}_j + J_3 \sum_{\langle\langle ij \rangle\rangle} \mathbf{S}_i \cdot \mathbf{S}_j, \quad (4.17)$$

and calculate the moment reduction at zero temperature by using the linearized spin-wave theory. Here, the first sum is taken over nearest-neighbor pairs, and the exchange constant is $J_{ij} = J_{xy}$ or $J_{ij} = J_{yz,zx}$ depending on the bond direction due to the underlying orbital ordering in Fig. 19(a). J_3 is the third-neighbor exchange coupling, shown in Fig. 8(b). Note that $J_{xy} \gg J_3$ are both antiferromagnetic, while $J_{yz,zx}$ is ferromagnetic and $|J_{yz,zx}| \ll J_{xy}$. Our calculations follow a standard procedure and the only special point in the calculations is a frustrated geometry of pyrochlore lattice and the anisotropic pattern of exchange couplings. The starting classical state is the one determined in the previous section and shown in Fig. 19(b). The magnetic unit cell has eight spins and we choose a pair of neighboring two tetrahedra (See Fig. 21). Quantum spin fluctuations around classical values are represented by the Holstein-Primakoff transformation in terms of boson operators. After inserting this for the Heisenberg model (4.17), we keep terms up to bilinear in boson operators and neglect higher-order terms. This bilinear boson Hamiltonian contains terms of boson-pair creation and annihilation and it is diagonalized by a Bogoliubov transformation. New boson operators defined in the Bogoliubov transformation describe magnetic excitations from the renormalized ground state. The moment reduction is represented by energy dispersion of these elementary excitations and matrix elements with original bosons introduced in the Holstein-Primakoff transformation, and is calculated in this way.

We show the moment reduction ΔS in Fig. 22 as a function of the third-neighbor exchange coupling J_3 . Here, we use $J_{xy} = 1$ along the xy chains and $J_{yz,zx} = -0.1$ along the yz or zx chains. The renormalized size of static magnetic moment is then given as $M_S = g\mu_B(S - \Delta S)$, where g and μ_B are g -factor and Bohr magneton, respectively, and we set an ordinary value $g = 2$, since the orbital magnetic moment is now quenched. As J_3 decreases, ΔS grows and diverges slowly in the $J_3 \rightarrow 0$ limit.

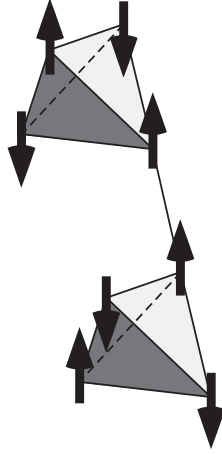
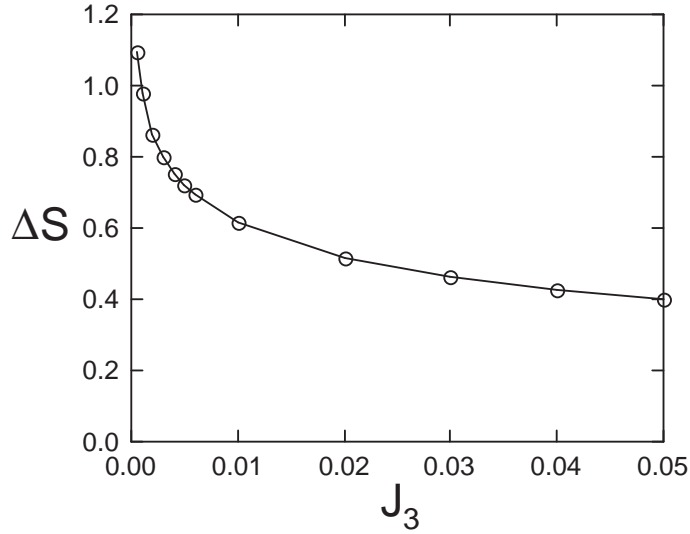


Fig. 21. Magnetic unit cell in the spin ordered phase.

Fig. 22. Moment reduction as a function of J_3 .

We show that this divergence is logarithmic in the following.

An essential point is the presence of zero modes at $J_3=0$. We show the dispersion relation of the lowest magnon mode along symmetric axes in the Brillouin zone at $J_3 = 0$ and 0.02 in Fig. 23. The magnon energy vanishes in two planes of $k_x = k_y$ and $k_x = -k_y$ as indicated in Fig. 23(a). Therefore, the magnon dispersion is one-dimensional at $J_3 = 0$ in this sense. As we discussed in a previous section, chains in the xy planes have large antiferromagnetic interchain couplings (J_{xy}) and these one-dimensional chains are weakly coupled with other chains in adjacent xy planes. Despite the presence of the weak ferromagnetic interplane couplings ($J_{yz,zx}$), magnons do not propagate along the z direction when $k_x = \pm k_y$. Each spin in xy chain is connected to two spins in a chain in an adjacent xy plane. Quantum inter-

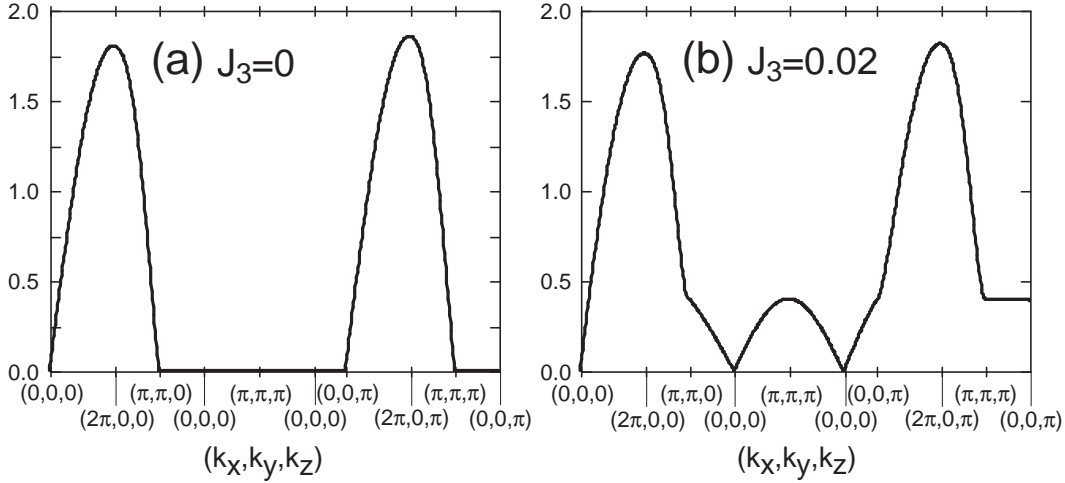


Fig. 23. The lowest magnon mode at (a) $J_3 = 0$ and (b) $J_3 = 0.02$.

ference of the two neighbor spins completely suppresses the propagation of magnon at these wavevectors, and this is also a manifestation of geometrical frustration effects of pyrochlore lattice. In the vicinity of $k_x = \pm k_y$ planes, the magnons of the lowest mode have a linear dispersion of energy, $\omega_{\mathbf{k}} \propto |\delta \mathbf{k}|$, where $|\delta \mathbf{k}|$ is the distance from the plane of $k_x = \pm k_y$. This leads to a logarithmic divergence in the moment reduction, $\Delta S \propto \log(\text{System Size})$. When the third-neighbor coupling J_3 is switched on, the zero modes acquire a finite energy that is proportional to J_3 as shown in Fig. 23(b). Therefore, the logarithmic divergence is cut off at this energy scale, resulting in $\Delta S \sim \log(1/J_3)$. From Fig. 22, for realistic value of $J_3 = 0.02J$, the moment reduction becomes $\Delta S \sim 0.5$. This leads to a largely reduced staggered moment $M_S \sim 1[\mu_B]$, which is consistent with experimental results.¹⁹⁾

§5. Discussion

5.1. Effect of relativistic spin-orbit coupling

Thus far, we neglected relativistic spin-orbit coupling, and employed the model that describes an interplay between the spin-orbital superexchange interactions and the cooperative Jahn-Teller coupling of tetragonal symmetry. We showed that the model successfully explains many experimental results of thermodynamic properties in vanadium spinel oxides. After our works, there have been complementary studies which theoretically examine effects of the relativistic spin-orbit coupling. Here, we briefly discuss about them in comparison with our work.

Tchernyshyov proposed a model assuming the dominant role of the relativistic spin-orbit coupling.¹⁶⁾ In his model, an effective angular momentum \mathbf{L}' with the magnitude $L' = 1$ is introduced to describe $(t_{2g})^2$ configurations. The orbital angular momentum is given by $\mathbf{L} = -\mathbf{L}'$, and couples to the $S = 1$ spin \mathbf{S} at each site antiferromagnetically, and consequently, the total momentum $\mathbf{J}' = \mathbf{L}' + \mathbf{S}$ with the magnitude $J' = 2$ is a conserved, good quantum number in the system. The

lowest energy state is the $J' = 2$ quintuplet. When the Jahn–Teller effect is included as a perturbation, a degeneracy remains partially in this manifold: The ground state energy is the same between $J'_z = 0$ state with an elongation of tetrahedron and $J'_z = \pm 2$ states with a compression of tetrahedron. Moreover, this degeneracy cannot be lifted even when the superexchange interactions are included. Consequently, the model fails to reproduce by itself the spin and orbital ordered state observed in experiments. By putting as an input the experimental fact that the magnetic ordering takes place, the model predicts the ground state with $J'_z = \pm 2$ and a compression of tetrahedron.

The orbital ordering predicted in this way is different from our result. In Tchernyshyov's model, the orbital occupation becomes uniform in space, that is, at all sites

$$\langle n_{i1} \rangle = \langle n_{i2} \rangle = \frac{1}{2}, \quad \langle n_{i3} \rangle = 1. \quad (5.1)$$

The orbital state is a complex one, $|d_{yz} \pm id_{zx}\rangle$ at all sites. On the other hand, our model predicts the A-type orbital ordering with a staggered occupation of d_{yz} and d_{zx} orbitals in the z direction as shown in Fig. 19(a). As pointed out in Ref. 16), the crystal symmetry is different between these two orbital states. The A-type ordering in Fig. 19(a) breaks mirror reflections in (110) and ($\bar{1}\bar{1}0$) planes as well as diamond glides in (100) and (010) planes, on the other hand, the uniform ordering in Eq. (5.1) preserves these symmetries.

Experimentally, the lattice symmetry below the structural transition temperature has not been completely determined yet. X-ray scattering results for polycrystal samples suggest the persistence of the mirror and glide symmetry at the low temperature phase.^{17),18)} On the contrary, recent synchrotron X-ray data for a single crystal sample suggest a breaking of the glide symmetry although they cannot decide whether the mirror symmetry is broken or not.¹⁹⁾ This controversy probably comes from a small electron–phonon coupling in this t_{2g} system. In order to settle the theoretical controversy, sophisticated experiments with large single crystals are highly desired.

Another model has been proposed by Di Matteo *et al.*¹³⁾ The model takes into account the spin–orbital superexchange interaction and the relativistic spin–orbit coupling on an equal footing. Mean–field analysis was applied to obtain the ground state. In the absence of the relativistic spin–orbit coupling, the ground state is the one shown in Fig. 5(b) for finite Hund's–rule coupling $\eta > 0$ as discussed in Sec. 3.2. When the relativistic spin–orbit coupling is turned on, the orbital state changes into a highly antisymmetric one (four sites in tetrahedron unit cell take different orbital states including both real and complex ones) with keeping the 3–up and 1–down spin configuration. Finally, for moderate values of the relativistic spin–orbit coupling, the ground state shows a transition into the spin and orbital ordered state which is compatible with Tchernyshyov's prediction by assuming the dominant relativistic spin–orbit coupling. In this sense, this study may interpolate our model and the Tchernyshyov's model. In their treatment, however, the Jahn–Teller coupling is completely neglected. As we have seen in Sec. 4.1, the mean–field ground states are drastically changed by the effects of the Jahn–Teller lattice

distortion. It is interesting to investigate with including the cooperative aspect of the lattice distortions.

5.2. Direction of magnetic moment

Experimentally, the spontaneous magnetic moment appears along the z direction. This is naturally explained by the scenario based on the relativistic spin-orbit coupling in the previous section as follows. The complex orbital state $|d_{yz} \pm id_{zx}\rangle$ has a finite matrix element of the z component of orbital angular momentum \mathbf{L} . This aligns the magnetic moment along the z direction through the spin-orbit coupling. On the other hand, the spin part of our model is completely isotropic, and no direction is preferred for spin ordering. Therefore, one needs to introduce a process with spin anisotropy to explain the observed spin direction. Here, we discuss that the direction of moment is reproduced by our model when we include quantum fluctuations in the orbital sector as well as the relativistic spin-orbit coupling in a perturbative way.

As described in Sec. 3.1, the orbital part of our model is completely classical, three-state clock type interaction, because we take into account the dominant σ -bond transfers only. If we include small contributions from π and δ -type transfer integrals, the orbital interaction is no longer classical, that is, contains small off-diagonal exchange interactions. This should lead to quantum fluctuations in the orbital sector. Our results in Sec. 4 showed that d_{xy} orbital is lowered and occupied at every site, and that d_{yz} and d_{zx} orbitals are alternatively occupied as long as the σ contribution is dominant. Under this situation, we expect that the orbital quantum nature, coming from small π and δ contributions, leads to fluctuations between d_{yz} and d_{zx} orbitals dominantly. This d_{yz} - d_{zx} fluctuation gives rise to a finite matrix element of L_z . As mentioned above, \mathbf{L} couples to the spin \mathbf{S} antiferromagnetically once we consider a finite relativistic spin-orbit coupling, and therefore, the induced L_z component aligns the magnetic moment in the z direction.

5.3. Weakly-coupled $S = 1$ chains — Haldane gap?

As discussed in Sec. 4, the orbital ordering reduces the magnetic frustration in our model. Below the orbital ordering temperature, antiferromagnetic correlations develop along the xy chains, and the coupling is frustrated between neighboring chains. Hence, the system can be regarded as weakly-coupled $S = 1$ spin chains under orbital ordering. It is well known that the ground state of antiferromagnetic $S = 1$ chain is spin-singlet, and a gap opens between the ground state and the lowest triplet excitation — the so-called Haldane gap.²⁰⁾ This is purely quantum mechanical effect, and hence it is beyond our present theory by mean-field argument and Monte Carlo simulation to examine the possibility of Haldane gap. Experimentally, vanadium oxides exhibit magnetically-ordered ground state, not the spin-singlet state, and we here address this issue in the light of our results and make some remarks.

It is known that the Haldane gap is fragile against the interchain couplings. For example, when antiferromagnetic $S = 1$ chains are connected to form of a simple cubic lattice structure, the critical value of the interchain exchange coupling is esti-

mated at 2 – 3% of the intrachain exchange coupling.²¹⁾ In our pyrochlore system, the relevant interchain coupling is the third-neighbor exchange J_3 in Fig. 8(a). The coupling J_3 constitutes a complicated three-dimensional network without any frustration among the chains. In addition, the neighboring xy chains are coupled by weak ferromagnetic coupling as well as second-neighbor coupling although they are frustrated due to the pyrochlore geometry. We expect for realistic parameter regime that the Haldane gap state is unstable against these interchain couplings.

On the other hand, as shown in the phase diagram in Fig. 20, the transition temperature for the magnetic ordering decreases rapidly as J_3 , and becomes zero in the limit of J_3 within our classical model. This implies that once all farther-neighbor couplings are irrelevant, a competition occurs between the long-range magnetic order and the quantum Haldane gap formation, leading to a quantum critical point. This interesting problem is left for further study.

§6. Summary

In this paper we have reviewed our recent studies on the geometrically frustrated systems, vanadium spinel oxides AV_2O_4 with divalent A -site cations. These are spin-1 antiferromagnets on the frustrated pyrochlore network of vanadium sites. We have employed an exchange model of electron spin and orbital degrees of freedom with including coupling to Jahn-Teller lattice distortion. By using mean-field approach and numerical calculations, we have shown that this model can describe two phase transitions in this system. The structural transition at a higher temperature is ascribed to orbital ordering accompanied by lattice distortion. The orbital ordering leads to an spatially anisotropic pattern of spin exchange couplings. Geometrical frustration of spins is thus relaxed, and this induces a magnetic transition. Spin configuration in the magnetic phase was determined and we found that it agrees with the one observed by neutron scattering experiments. It was also found that the third-neighbor spin exchange couplings are important to determine the spin configuration and the magnetic transition temperature. A realistic value of the third-neighbor coupling gives a size of the magnetic moment and a transition temperature, both of which are quite well in agreement with the experimental values. These semiquantitatively good agreements with experimental results support our choice of model Hamiltonian and also our picture of the two transitions. A few points, however, remain to be investigated in more details. One is more systematic analysis of the Jahn-Teller effects. So far, we have considered only uniform modes of lattice distortion, experimentally observed ones, but it is important to check that the uniform mode is the most unstable one. Another point is more quantitative analysis of the effects of transverse orbital fluctuations. These are introduced by electron hoppings in π - and δ -bonds. The orbital part of the effective exchange model remains strongly anisotropic of three-state Potts type even with including transverse orbital couplings, but it is interesting to investigate the effects of these couplings. The transverse couplings induce orbital angular momentum, and therefore the relativistic spin-orbit coupling may show interesting effects.

Acknowledgements

We would like to thank M. Onoda and S.-H. Lee for fruitful discussions. Y. M. would like to thank D.I. Khomskii, G. Jackeli and C. Yasuda for helpful comments. This work was supported under a Grant-in-Aid for Scientific Research (No. 16GS50219) and NAREGI from the Ministry of Education, Science, Sports, and Culture of Japan

References

- 1) H. Tsunetsugu and Y. Motome, Phys. Rev. B **68** (2003), 060405(R).
- 2) Y. Motome and H. Tsunetsugu, Phys. Rev. B **70** (2003), 184427.
- 3) Y. Motome and H. Tsunetsugu, Physica B **359-361** (2005), 1222.
- 4) Y. Motome and H. Tsunetsugu, J. Phys. Soc. Jpn. **74** Suppl. (2005), 208.
- 5) Y. Motome, H. Tsunetsugu, T. Hikihara, N. Shannon and K. Penc, preprint (cond-mat/0506598).
- 6) Y. Ueda, N. Fujiwara and H. Yasuoka, J. Phys. Soc. Jpn. **66** (1997), 778.
- 7) Y. Tokura and N. Nagaosa, Science **288** (2000), 462, and references therein.
- 8) Muhtar, F. Takagi, K. Kawakami and N. Tsuda, J. Phys. Soc. Jpn. **57** (1988), 3119.
- 9) S. Niziol, Phys. Status Solidi A **18** (1973), K11.
- 10) W. A. Harrison, *Electronic Structure and the Properties of Solids* (Dover, 1980).
- 11) J. Matsuno, A. Fujimori and L. F. Mattheiss, Phys. Rev. B **60** (1999), 1607.
- 12) K. I. Kugel and D. I. Khomskii, Zh. Eksp. Teor. Fiz. **64** (1973), 1429 [Sov. Phys. JETP **37** (1973), 725]; Fiz. Tverd. Tela, **17** (1975), 454 [Sov. Phys. Solid State **17** (1975), 285].
- 13) S. Di Matteo, G. Jackeli and N. B. Perkins, Phys. Rev. B **72** (2005), 020408(R).
- 14) Y. Yamashita and K. Ueda, Phys. Rev. Lett. **85** (2000), 4960.
- 15) J. Villain, J. Phys. C: Solid State Phys. **10** (1977), 1717; Z Phys. B **33** (1979), 31.
- 16) O. Tchernyshyov, Phys. Rev. Lett. **93** (2004), 157206.
- 17) N. Nishiguchi and M. Onoda, J. Phys: Condens. Matter **14** (2002), L551; M. Onoda and J. Hasegawa, *ibid.* **15** (2003), L95.
- 18) M. Reehuis, A. Krimmel, N. Büttgen, A. Loidl and A. Prokofiev, Eur. Phys. J. B **35** (2003), 311.
- 19) S.-H. Lee, D. Louca, H. Ueda, S. Park, T.J. Sato, M. Isoba, Y. Ueda, S. Rosenkranz, P. Zschack, J. Iniguez, Y. Qiu and R. Osborn, Phys. Rev. Lett. **93** (2004), 156407; S.-H. Lee, private communication.
- 20) F. D. M. Haldane, Phys. Lett. **93A** (1983), 464; Phys. Rev. Lett. **50** (1983), 1153.
- 21) A. Koga and N. Kawakami, Phys. Rev. B **61** (2000), 6133; C. Yasuda, S. Todo, K. Hukushima, F. Alet, M. Keller, M. Troyer and H. Takayama, Phys. Rev. Lett. **94** (2005), 217201.